Charge Transfer in InAs@ZnSeMoS2 Heterostructures for Broadband Photodetection

ADVANCED FUNCTIONAL MATERIALS
www.afm-journal.de

Charge Transfer in InAs@ZnSe-MoS_2 Heterostructures for Broadband Photodetection

*Aswin Asaithambi, Mukesh Kumar Thakur, Dongxu Zhu, Nastaran Kazemi Tofighi, Jacopo Stefano Pelli Cresi, Sidharth Kuriyil, Nicola Curreli, Nicolò Petrini, Luca Rebecchi, Luca De Trizio, Andrea Toma, Liberato Manna, and Ilka Kriegel**

Absorbing near-infrared (NIR) photons, with longer wavelengths, in atomically thin monolayer MoS_2 presents a significant challenge due to its weak optical absorption and narrow absorption bands. Consequently, MoS_2-based photodetector devices often experience low responsivity and a limited detection window. Herein, a novel InAs@ZnSe core@shell/1L-MoS_2 heterostructure, leveraging InAs@ZnSe as the primary infrared-absorbing material and exploiting the formation of a type-II heterostructure is showcased. Steady-state and time-resolved spectroscopy, along with optoelectronic characterization, are employed to investigate photo-induced charge transfer dynamics. The results show efficient hole transfer to InAs@ZnSe upon excitation of both materials. Instead, with selective excitation of InAs@ZnSe, electron transfer is observed from InAs@ZnSe to the 1L-MoS_2. The heterostructure demonstrates a broadband photoresponse spanning the wavelength range of 300 to 850 nm, exhibiting a Responsivity of $\approx 10^3$ A/W and Detectivity of $\approx 10^{11}$ Jones. The signal-to-noise ratio substantially increases by 3 to 4 orders of magnitude for 700 and 850 nm excitation compared to pristine 1L-MoS_2. The enhancement in photoresponse and signal-to-noise ratio is attributed to increased absorption, which helps eliminate defect and trap states, thereby promoting the photogating effect.

1. Introduction

Transition metal dichalcogenides (TMDCs) have attracted great attention in the past decades, particularly after the discovery of graphene.[1–5] The presence of bandgap and layered structure of these TMDCs provides a unique platform to tune optical and electrical properties.[6–8] For example, monolayer MoS_2 has a direct band gap, whereas the multilayer form exhibits an indirect band gap.[9] Monolayer TMDCs possess unique electronic and optical properties, which have paved the way for numerous applications in optoelectronics, photonics, and energy storage devices.[1,2,10] The atomically thin layers of these TMDCs pose challenges in effectively absorbing light as a result of their thin and defect-prone nature.[11–13] Consequently, photodetector devices based on TMDCs frequently exhibit very low photoresponse and a limited detection window due to their bandgap (for MoS_2, this threshold is 680 nm).[14,15]

A. Asaithambi, M. K. Thakur, N. K. Tofighi, S. Kuriyil, N. Curreli, N. Petrini, L. Rebecchi, I. Kriegel
Functional Nanosystems
Italian Institute of Technology
via Morego 30, Genoa 16163, Italy
E-mail: ilka.kriegel@polito.it

D. Zhu, L. De Trizio, L. Manna
Nanochemistry
Italian Institute of Technology
via Morego 30, Genoa 16163, Italy

The ORCID identification number(s) for the author(s) of this article can be found under https://doi.org/10.1002/adfm.202409951

N. K. Tofighi
Physics and Chemistry of Nanostructures Group
Department of Chemistry and NOLIMITS
Core Facility for Non-Linear Microscopy and Spectroscopy
Ghent University
Ghent 9000, Belgium

J. S. Pelli Cresi, A. Toma
Clean Room facility
Italian Institute of Technology
Via Morego 3, Genoa 10129, Italy

S. Kuriyil, L. Rebecchi, I. Kriegel
Dipartimento di Scienza Applicata e Tecnologie (DISAT)
Politecnico di Torino
Corso Duca degli Abruzzi 24, Torino 10129, Italy

N. Curreli
Swiss Federal Laboratories for Materials Science and Technology
Überlandstrasse 129, Dübendorf 8600, Switzerland

DOI: 10.1002/adfm.202409951

Several strategies have been documented in the last few years to increase optical absorption and extend the light detection window.[16,17] These strategies mainly include coupling of TMDCs with plasmonic nanomaterials, strain engineering, and coupling TMDCs with low-dimensional materials. Coupling TMDCs with plasmonic nanomaterials offers the major advantage of enhancing light-matter interaction.[13,16–20] However, the optical absorption of the plasmonic nanomaterials remains a major challenge, limiting the detection window.[13,18,21,22] Strain engineering also helps to increase the detection wavelength. Recently, Liu et al. proposed the strain-plasmonic coupling effect with MoS_2, enabling detection up to 740 nm with a very high signal-to-noise ratio (650%) compared to pristine MoS_2.[23] Coupling TMDCs with low-dimensional materials involves using the latter as photo-absorbing materials to enhance absorption and detection wavelength.[24,25] For instance, Kufer et al. proposed a hybrid 2D–0D (MoS_2-PbS) structure,[26] and their device exhibited record responsivity $>10^5$ higher than what can be achieved individually by PbS quantum dots and MoS_2-based photodetectors.[26] However, in this configuration, a very high gate voltage (−100 V) was applied along with the use of toxic PbS.[26] Similarly, Sahatiya et al. proposed a 2D MoS_2-carbon quantum dot hybrid structure for broadband photodetection, achieving detection up to 780 nm with observed device photoresponsivity in the order of mA/W.[27] The integration of low-dimensional materials is not limited to only TMDCs; it is also possible to integrate these materials with existing technologies like those based on silicon.[28–30] For example, Pal et al.[29] have demonstrated wafer-scale MoO_3/MoS_2/Si heterojunctions for wavelength-selective photodetection applications in the spectral range of 400–700 nm. This was achieved using variable-sized MoO_3/MoS_2 colloidal core-shell quantum dots (QDs) and adjusting the oxide shell-to-core thickness ratio.[28,29]

The 0D–2D configuration offers a low-cost solution coating process, facilitating the creation of hybrid structures.[31–34] However, it is important to note that both 0D and 2D materials have limitations in optical absorption, quantum efficiency, and other parameters.[35,36] Indium arsenide (InAs) has recently garnered significant attention in infrared technology due to its tunable IR absorption, high quantum efficiency, and compliance to the European Union's "Restriction of Hazardous Substances" (RoHS) directives.[35–39] Recently, Ning et al.[40] reported computational investigations of the interfacial InAs/MoS_2 heterostructure (HS). They proposed a larger redistribution of charges, a strong interfacial interaction, and an improved absorption of light in InAs/MoS_2 heterostructure compared to only MoS_2.[40] However, to the best of our knowledge, experimental work on InAs/MoS_2 heterostructure has not been reported, especially concerning InAs nanocrystals and MoS_2 monolayers. In this work, we fabricated an InAs@ZnSe/MoS_2 HS using mechanically exfoliated monolayer MoS_2 (monolayer MoS_2 referred as 1L-MoS_2)and InAs@ZnSe colloidal core@shell nanocrystals (henceforth referred to as "InAs@ZnSe NCs"). Coupling of InAs@ZnSe NCs with MoS_2 results in a charge transfer between both materials upon optical excitation of either single or both materials. From our findings, supported by the reported literature,[39] we could confirm a type II band-alignment of the heterostructure. We employed steady-state, time-resolved spectroscopy, and photocurrent measurement techniques to probe the photo-induced charge transfer processes. The results show hole transfer to InAs@ZnSe NCs upon excitation of both materials and with selective excitation of InAs@ZnSe NCs, electron transfer from InAs@ZnSe NCs to the MoS_2. The InAs@ZnSe/ MoS_2 HS is implemented, which exhibits a broadband photoresponse from 300 to 850 nm with a maximum responsivity of 4276 A/W and detectivity (D^*) 10^{11} Jones for the InAs@ZnSe/MoS_2 HS at a wavelength of 700 nm, in comparison to pristine 1L-MoS_2. The signal-to-noise ratio increases by 3 to 4 orders of magnitude for 700 and 850 nm excitation compared to monolayer MoS_2. The increment in detection range, higher responsivity compared to the single layer MoS_2, and improvement in the signal-to-noise ratio are attributed to the photoinduced interaction of InAs@ZnSe NCs with MoS_2, which broaden the absorption window of 1L-MoS_2, thus increasing the overall absorption and the removal of defect and trap states, promoting the photogating effect. Our study highlights the potential applications in optoelectronic devices, with fundamental photophysics providing a pathway to integrate 2D semiconductors with 0D InAs NCs materials for future infrared technologies.

2. Result and Discussion

InAs@ZnSe core@shell nanocrystals (InAs@ZnSe NCs) were synthesized using the experimental procedure recently reported by our group.[38,41] In detail, InAs@ZnSe NCs were produced by employing $ZnCl_2$ as an additive, tris(dimethylamino)arsine as the As precursor, and alane N,N-dimethylethylamine as the reducing agent. The reaction was performed at 300 °C for 15 min, after which it was quenched, and the shelling process was carried out in situ by adding tri-n-octylphosphine-Se (1 M) and heating up the system at 300 °C for 10 min. As synthesized InAs NCs are ≈ 6 nm in size, based on transmission electron microscopy (TEM) analysis (**Figure 1a**). The details regarding the shell thickness and chemical composition are provided in Table S1 (Supporting Information Section 1) and are also reported in our previous work[38,41]

InAs NCs exhibit excitonic absorption at ≈835 nm and emission at ≈935 nm (Figure 1b). The MoS_2 monolayer was fabricated using the Au-assisted exfoliation technique.[42–44] A detailed description of the exfoliation process is provided in Figure S1 (Supporting Information Section 1.1), along with the overall device fabrication procedure. The Au-assisted exfoliation technique offers a broader platform for achieving large-area exfoliation of 2D materials.[45]

The optical image of a large area of MoS_2 is shown in Figure 1c, where the monolayer MoS_2 is marked in a white circle and represented as 1L-MoS_2, and only the substrate SiO_2/Si is shown in a yellow dotted line for clarity. The 1L-MoS_2 is not present everywhere; the darker contrast indicates regions with few or multiple layers of MoS_2 (indicated by a black arrow). Additionally, we performed Atomic Force Microscopy (AFM) to measure the thickness of the monolayer, which was found to be ≈0.9 nm (Figures S2a,b Supporting Information) and is in good agreement with previous work.[46,47]

The colloidal InAs@ZnSe NCs were spin-coated onto the MoS_2 to form a uniform single layer of InAs@ZnSe NCs on top of both 1L-MoS_2 and the substrate (SiO_2/Si).

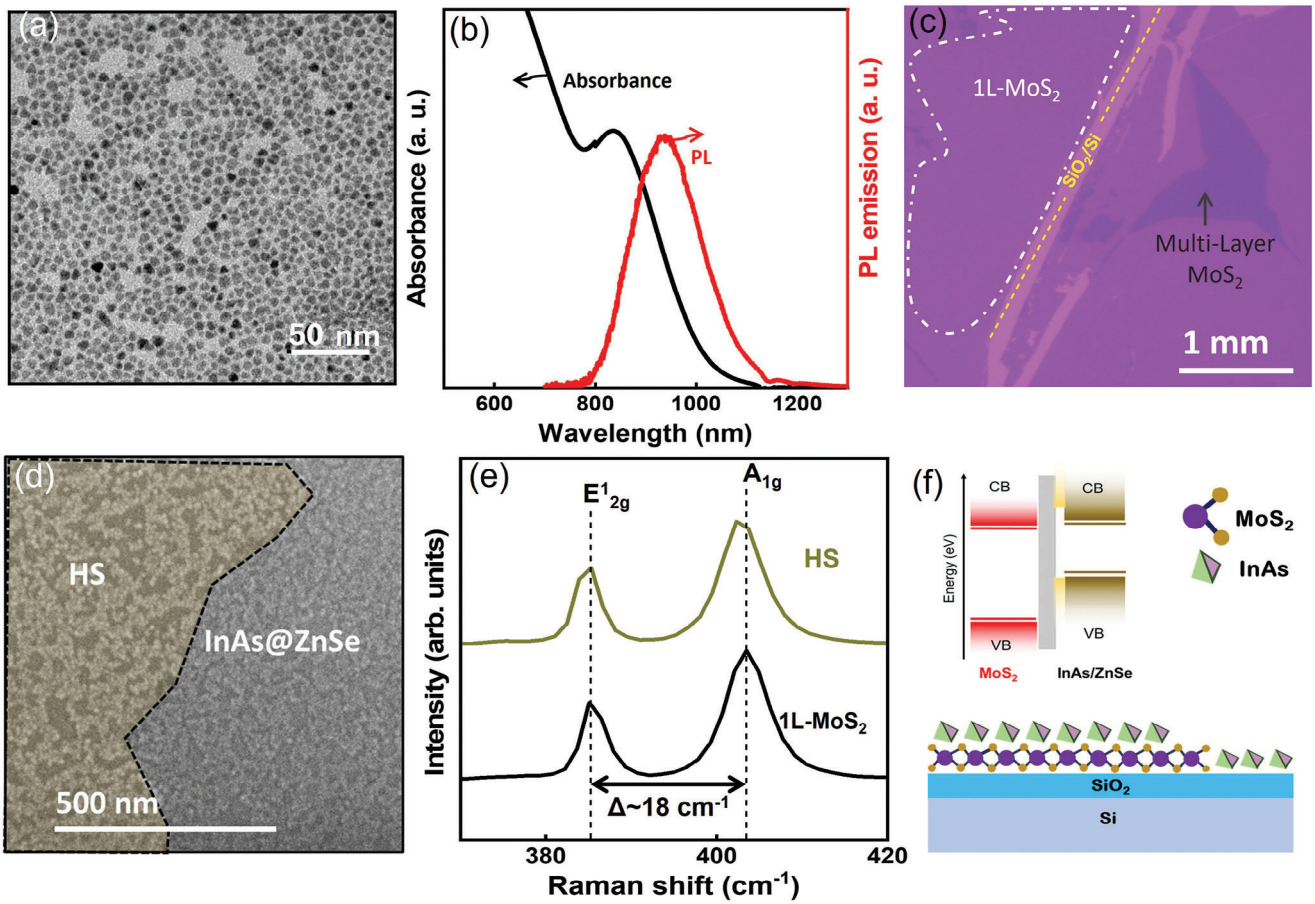

Figure 1. a) Transmission electron microscope (TEM) image of InAs NCs shell. b) Absorption (black curve) and photoluminescence (PL) (red curve) spectra of as-synthesized InAs nanocrystals in solution. c) Optical image of Au-assisted MoS_2 on a SiO_2/Si substrate. The monolayer (1L) MoS_2 is marked with a white circle, while an arrow indicates the bulk or multilayer MoS_2. d) The SEM image displays an area covered with InAs@ZnSe nanocrystals shaded in grey, while the InAs@ZnSe/MoS_2 heterostructure (HS) is marked in yellow for clarity. e) Raman spectra of MoS_2 (black curve) and InAs@ZnSe/MoS_2 (grey) HS samples under 532 nm excitation (power 0.3 mW) with the same conditions. f) Schematic illustration of InAs@ZnSe NCs and 1L-MoS_2 HS, along with energy level diagrams of 1L-MoS_2 and InAs@ZnSe NCs before contact, representing the type II band alignment.

Figure 1d shows a scanning electron microscope (SEM) image of InAs@ZnSe/MoS_2 heterostructure (HS), with an area covered by a uniform layer of InAs@ZnSe NCs shaded in grey, while the InAs@ZnSe/MoS_2 HS is marked in yellow. To estimate the thickness of the InAs@ZnSe/MoS_2 HS, we performed AFM measurements, which revealed a thickness of ≈10 nm, as shown in Figures S2c,d (Supporting Information). For other high-resolution SEM images of InAs@ZnSe/MoS_2 HS with discussion provided in Figure S3a–f (Supporting Information, Section 1.3). It is crucial to ensure that the heterostructure contains minimal or no non-interacting InAs@ZnSe NCs, as their presence can adversely affect the desired properties and performance. Raman spectroscopy with the high spectral resolution was performed on pristine1L-MoS_2 and the InAs@ZnSe/MoS_2 HS under identical conditions (i.e., employing a 532 nm laser excitation). Two characteristic Raman peaks, E^1_{2g}, and A_{1g}, arise from the in-plane and out-of-plane modes of MoS_2, as illustrated in Figure 1e. The separation between E^1_{2g} and A_{1g} for pristine MoS_2 is ≈18 cm^{-1} (Figure 1e), further confirming the monolayer nature of the MoS_2 flake and agrees well with the previous report.[43,48,49] The peak position of the E^1_{2g} mode for pristine MoS_2 and InAs@ZnSe/MoS_2 HS is ≈386.47 and 386.12 cm^{-1}, respectively, while for A_{1g}, it is 404.20 cm^{-1} for MoS_2 and 404.40 cm^{-1} for InAs@ZnSe/MoS_2 HS. In the case of the InAs@ZnSe/MoS_2 HS, both the A_{1g} and E^1_{2g} peaks exhibit no significant shift, indicating that the crystalline nature of the 1L-MoS_2 is preserved. A small fluctuation in the A_{1g} mode (Figure 1e, HS spectra) is noted, but it is within the instrument's margin of error.[49] The integration of InAs@ZnSe NCs with 1L-MoS_2 could lead to a type II energy band alignment, attributed to the differences in work functions for 1L-MoS_2[50] and InAs@ZnSe NCs[39,49–52] as illustrated in the schematic shown in Figure 1f. The InAs@ZnSe/MoS_2 HS were then investigated using steady-state photoluminescence (PL) spectroscopy in ambient conditions. InAs@ZnSe NCs show PL ≈ 1.5 eV (950 nm) as shown in **Figure 2**a blue curve and 1L-MoS_2 exhibits photoluminescence (PL) with two distinct peaks, as shown in the blue curve of Figure 2b. The lower energy peak at 1.82 eV (670 nm) is the A exciton, originating from the direct electron transition from the valence band maximum to the conduction band minimum at the K or K' point of the Brillouin zone. The higher energy peak at 1.95 eV (630 nm) is the B exciton, resulting

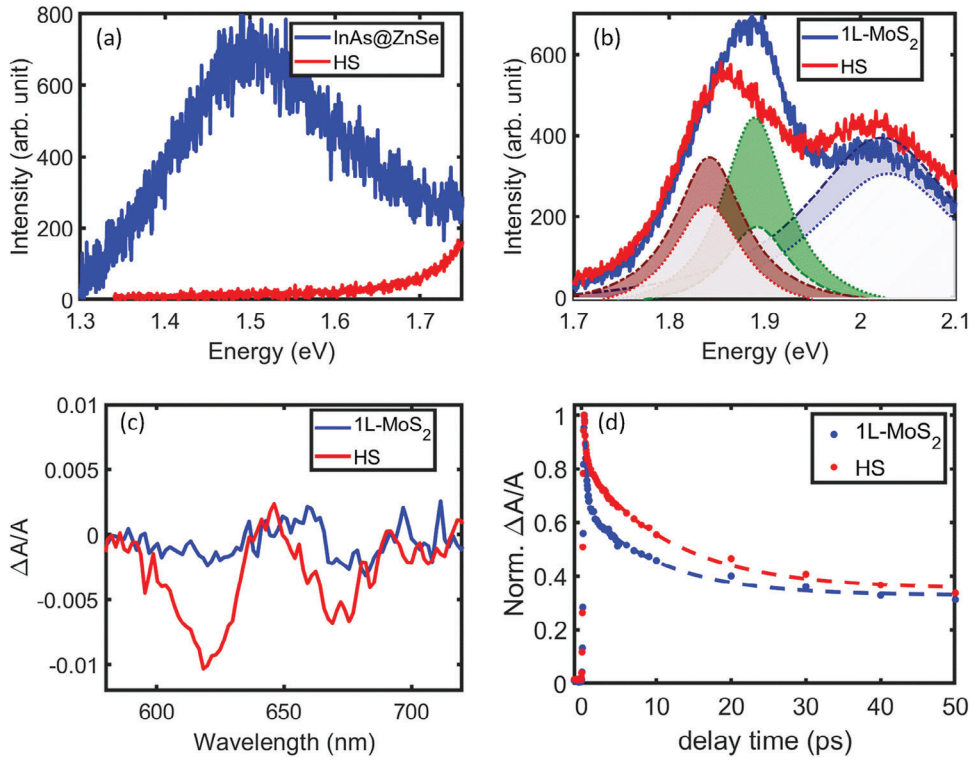

Figure 2. a) Photoluminescence spectra of InAs@ZnSe NCs (blue curve), and HS (red curve) under the 532 nm excitation show quenching of InAs@ZnSe emission. b) Photoluminescence spectra of MoS_2 (blue curve) and HS (red curve) also show quenching of 1L-MoS_2 emission (532 nm excitation, excitation power of 500 µW, and 5 s integration time). 1L-MoS_2 PL was deconvoluted into B exciton (dark blue), A exciton (dark green), and A trion (dark red) by fitting with three Lorentz functions. c) Transient absorption spectra of 1L- MoS_2 (blue curve) and HS (red curve) at 1 ps delay time with 800 nm pump (pump power of 100 µW, at 50 KHz and 120 µm spot size). d) Transient absorption decay of A exciton in 1L-MoS_2 (blue curve) and HS (red curve) with 532 nm pump (pump power of 50 µW, at 50 kHz and 120 µm spot size), both decays were fitted with bi-exponential decay function.

from the electron transition from the spin-orbit split valence band maximum to the conduction band minimum at the K' or K point.[53,54]

The PL from both InAs@ZnSe NCs and 1L-MoS_2 were quenched upon excitation of both components with 532 nm light in the heterostructure configuration. Figure 2a shows a complete quenching of the PL from the InAs@ZnSe NCs (between 1.4 to 1.6 eV) in the HS (red curve) compared to InAs@ZnSe NCs on a Si/SiO_2 substrate (blue curve). Figure 2b shows the PL of 1L-MoS_2 on the SiO_2/Si substrate (blue curve) and on the HS (red curve), a partial quenching along with a red shift with the A exciton ≈1.82 eV (670 nm) and B exciton is observed ≈1.95 eV (630 nm) which is also indicative of monolayer nature of MoS_2.[32] The PL quenching in both materials could indicate charge transfer within the InAs@ZnSe/MoS_2 HS and suggest type-II band alignment. Previous reports suggest that PL red shifting and quenching in MoS_2 may result from the n-type doping effect due to specific band alignment at the interface and the formation of trions.[54,55] To gain further understanding of the charge transfer and photoluminescence (PL) quenching mechanisms, we have deconvoluted and fitted the 1L-MoS_2 and InAs@ZnSe/MoS_2 HS PL spectra, as shown in Figure 2b. 1L-MoS_2 PL is a combination of exciton (X_0) and trion (X_T) emission with $E(X_0) > E(X_T)$.[56] The equilibrium of exciton (n_X), trion (n_T), and free carriers (n_e) follows a Boltzmann distribution at low excitation densities, as shown in Equation (1):[57–59]

$$\frac{n_X n_e}{n_T} = \frac{4 m_X m_e}{\pi h^2 m_T} . k_B T \exp\left(-\frac{E_B}{k_B T}\right) \quad (1)$$

where m_e is the effective mass of the electron, $m_{X,}$ and m_T are the effective masses of the exciton and trion, respectively, T is the temperature and E_B is the intrinsic trion binding energy.

By employing Lorentzian fitting, we calculated the variation in free carrier density (n_e) based on the densities of excitons (X_0) and trions (X_T) in both 1L-MoS_2 and the InAs@ZnSe/MoS_2 HS. Remarkably, in the case of the InAs@ZnSe/MoS_2 HS, the n_e increases by eightfold compared to 1L-MoS_2 alone. This increase in n_T was observed across the whole flake (Figure S4 (Supporting Information).

Upon photoexcitation with a 532 nm light source, n-doping of MoS_2 is observed potentially due to both electron transfer processes to 1L-MoS_2 and hole transfer to InAs@ZnSe NCs in the HS. To further investigate the charge transfer processes in InAs@ZnSe/MoS_2 HS, transient absorption pump-probe spectroscopy was used.[60] The broadband transient absorption map is obtained by measuring the variation of supercontinuum source transmitted via both 1L-MoS_2 and InAs@ZnSe/MoS_2 HS on

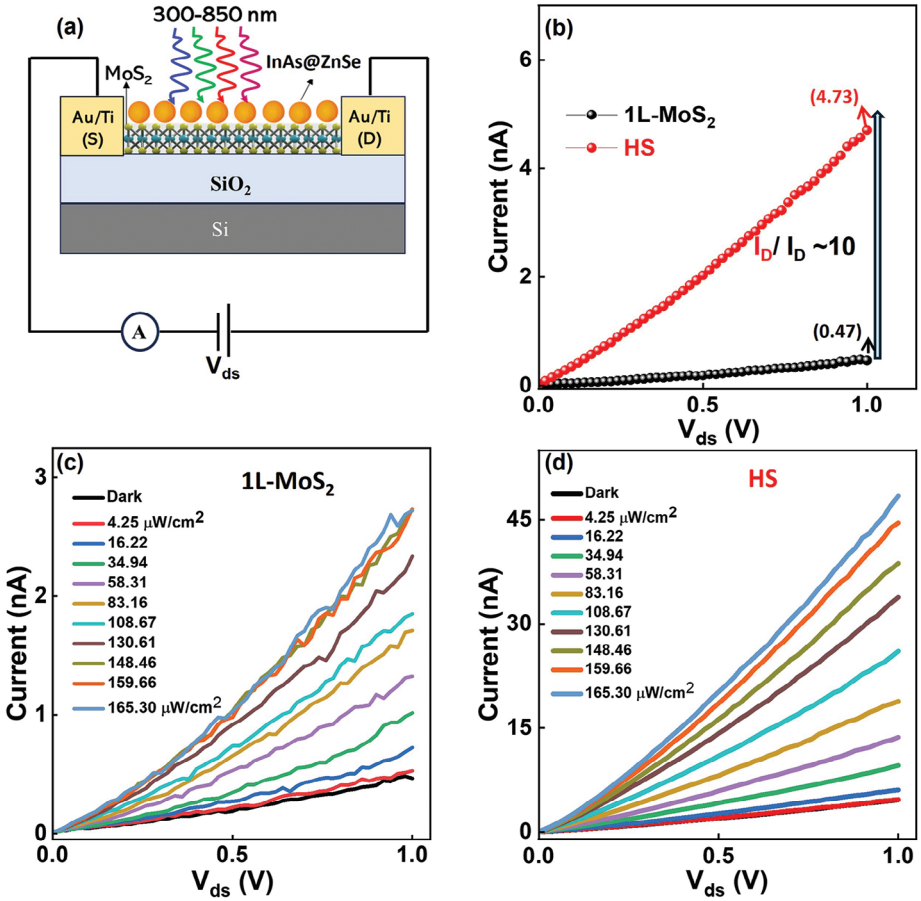

Figure 3. a) Schematic illustration of the InAs@ZnSe/MoS_2-based HS consisting of monolayer MoS_2 and InAs@ZnSe nanocrystals. b) Dark I–V characteristics of the MoS_2 and InAs@ZnSe/MoS_2 HS device. I–V characteristics of the c) pristine 1L-MoS_2 and d) InAs@ZnSe/MoS_2 HS under 532 nm excitation with increasing excitation power density. The power density values are indicated according to the color coding in panels c and d.

SiO_2 substrate after 532 nm and 800 nm excitation. In this setup, the 532 and 800 nm wavelengths serve as the pump sources, initiating the photoexcitation process. Meanwhile, broadband white light is employed as the probe. The details about experimental setup and other parameters are provided in the experimental section. We mainly look at the excitons of 1L-MoS_2 and specifically the A exciton of 1L-MoS_2 to identify the charge transfer processes. The transient absorption map of 1L- MoS_2 under above bandgap excitation with 532 nm shows a typical bleach signal of the excitonic peaks labeled as A (≈ 670 nm) and B (≈ 630 nm)[60] as shown in Figure S5 (Supporting Information). In the case of below band gap excitation of 1L-MoS_2 (at 800 nm) a very weak noisy data (blue curve in Figure 2c) is observed, indicating a weak interaction of the pump with the sample system.[43] Interestingly, in the case of the InAs@ZnSe/MoS_2 HS under 532 nm excitation (Figure S5d, Supporting Information), slightly more intense bleaching is observed along with slightly longer decay of A exciton compared to the signal from 1L-MoS_2 (see Figure 2d). The decay is fitted with a biexpoential function that includes fast and slow components; the observed values of fast and slow components are 0.29 and 10 ps for 1L-MoS_2 and 0.27 and 12 ps for the InAs@ZnSe/MoS_2 HS, respectively. The sub picosecond times (fast component) indicate the formation time of excitons in 1L-MoS_2, while the longer time (slow component) is correlated to the exciton lifetimes. The weight of the fast component is reduced from 52% to 37% in the InAs@ZnSe/MoS_2 HS, indicating a competing process such as charge transfer.[61,62] These observations are indicative of charge transfer processes occurring from InAs@ZnSe to 1L-MoS_2 and vice versa, as also suggested by the PL data (Figure 2b). The 532 nm excitation wavelength is above the band gap for both materials (InAs@ZnSe and 1L-MoS_2), causing them to absorb light and transfer charge carriers to each other. This results in the ground state depletion, which manifests as the negative signal observed in the transient absorption map. Notably, after selective excitation of InAs@ZnSe NCs in the HS with 800 nm excitation, bleaching of A and B exciton states of 1L-MoS_2 is observed (Figure S5, Supporting Information), despite the below gap excitation. This observation suggests that InAs@ZnSe NCs absorb the 800 nm light and transfer electrons to 1L-MoS_2.[60] Following spectroscopic verification, we proceeded with the electrical characterization of the InAs@ZnSe/MoS_2 HS. Our objective was to explore the correlation of charge transfer at higher wavelengths between InAs@ZnSe NCs and 1L-MoS_2. The schematic illustration of the InAs@ZnSe/MoS_2 HS is depicted in **Figure 3a**, with comprehensive details of the HS implementation provided

in Figure S1 (Supporting Information Section 1.1). Initially, we examined the photoconductivity of pure 1L-MoS_2 devices under various excitations ranging from 300–850 nm. InAs@ZnSe NCs were then spin-coated onto the same 1L-MoS_2 flake, as illustrated in Figure 3a. The details about HS implementation are provided in Section 1.1 (Supporting Information).

The dark I_{ds}-V_{ds} characteristics of 1L-MoS_2 and InAs@ZnSe/MoS_2 HS are depicted in Figure 3b. The drain current for pristine 1L-MoS_2 is considerably lower than that of the InAs@ZnSe/MoS_2 HS, which experiences a significant increase (approximately ten-fold). The lower drain current (higher resistance) in pristine 1L-MoS_2 is due to surface adsorbates and defect states, as discussed in previous reports.[63–65] This surge in dark current can be ascribed to doping (Figure 2b)[56] and passivation arising from the deposition of InAs@ZnSe on the 1L-MoS_2, a concept elucidated in our prior research.[57] In detail, 1L-MoS_2 possesses various defects and trap states, such as sulfur and molybdenum vacancies, which make it highly sensitive to O_2 and H_2 adsorption.[66] Coating 1L-MoS_2 with InAs@ZnSe NCs effectively passivates its surface defects and prevents direct exposure to O_2/H_2 environments, an aspect which will be discussed later.[66] A similar observation was reported by Li et al., who utilized gold chloride hydrate to dope MoS_2.[67] Their results demonstrated an approximately 32-fold increase in dark current.[67] The power dependence of the I_{ds}–V_{ds} curve for pristine 1L-MoS_2 and InAs@ZnSe/MoS_2 HS under the 532 nm excitation is illustrated in Figure 3c,d. As we increase the power densities from 4.25 to 165.3 μW cm^{-2}, the drain current experiences a substantial increase at a different bias voltage of 0 to 1 V. For 1L-MoS_2, the drain current rises from 0.53 to 2.7 nA, whereas for InAs@ZnSe/MoS_2 HS it varies from 4.70 to 48 nA at bias voltage 1 V. The power-dependent photocurrent ($\Delta I = I_{light} - I_{dark}$) of InAs@ZnSe/MoS2 HS as a function of voltage at various wavelengths is provided in Figure S6 (Supporting Information).

The dynamic photoresponse (I–t) characteristics of both pristine 1L-MoS_2 devices and InAs@ZnSe/MoS_2 HS were investigated under various excitations ranging from 300 to 850 nm, as depicted in **Figures** 4a (also Figuresa,b S7 a,b, Supporting Information) and Figure 4b. 1L-MoS_2 exhibits a significant photocurrent in the UV and visible regions.[49] However, when excited with a 700 nm wavelength at maximum power (0.7 mW cm^{-2}), the device shows a very poor signal, and further increasing the wavelength to 850 nm results in the photocurrent being undetectable. This behavior is anticipated since the optical absorption cutoff window of pristine 1L-MoS_2 extends up to 680 nm, as documented in prior studies.[14,23] Interestingly, adding InAs@ZnSe NCs onto the 1L-MoS_2 surface (InAs@ZnSe/MoS_2 HS) leads to a notable enhancement in the photocurrent observed across the entire wavelength range from 300 to 850 nm, as shown in Figure 4b. The expansion of the detection window beyond 680 nm can be readily explained by the significant absorption characteristics of InAs@ZnSe NCs in the infrared region.[36,39,41] The multiple dynamic photoresponse and power dependency of the InAs@ZnSe/MoS_2 HS are presented in Figures S8 and S9 (Supporting Information), respectively. These figures demonstrate the excellent stability and reproducibility of the switching behavior of the InAs@ZnSe/MoS_2 HS under different wavelengths. To further explore signal detection, including in the infrared range, we calculated the signal-to-noise ratios (SNRs) using the formula[23,68] ($SNRs = (I_{light} - I_{dark})/I_{dark}$) as shown in Figure 4c. Our observations revealed that the InAs@ZnSe/MoS_2 HS exhibits superior SNRs compared to pristine 1L-MoS_2. Notably, at 700 nm, the SNRs percentage increased by approximately 3 orders of magnitude, and at 850 nm, by approximately 4 orders of magnitude, surpassing all previous reports.[23] The multiple dynamic photo responses under 850 nm excitation are depicted in Figure 4d, where "ON" indicates that the light is falling on the device, and "OFF" indicates that the light is switched off. The multiple switching characteristics demonstrate that the InAs@ZnSe/MoS_2 HS exhibits high stability under 850 nm. For a comprehensive understanding of the performance of the InAs@ZnSe/MoS_2 HS, key parameters such as responsivity (R) and detectivity (D^*) are calculated using the formula provided below:

$$R = \frac{\Delta I}{P} \tag{2}$$

$$D^* = \frac{R\sqrt{A}}{\sqrt{2eI_d}} \tag{3}$$

where ΔI is the photocurrent, and P is the power density. A is the active area of the device, e is the electronic charge, and I_d is the dark current.

The values of R as a function of different wavelengths for pristine 1L-MoS_2 and InAs@ZnSe/MoS_2 HS are depicted in **Figure** 5a. As explained above, the spectral variation in R demonstrates that 1L-MoS_2 exhibits a weak response at higher wavelengths. Interestingly, in the case of InAs@ZnSe/MoS_2 HS, the overall response is increased compared to pristine 1L-MoS_2, with the device showing very high photoresponse at 700 nm. The value of R for 1L-MoS_2 and InAs@ZnSe/MoS_2 HS at 700 nm (V_{ds} = 1 V and power density = 0.7 mW cm^{-2}) is 1.35 and 1557.6 A/W, respectively, and for 850 nm, pure 1L-MoS_2 is ≈0.05 mA/W, while InAs@ZnSe/MoS_2 HS is at 10.58 A/W (The detailed calculation is provided in the section 1.10 Supporting Information). The variation in R as a function of power density is shown in Figure 5b. As we increased the power, the responsivity decreased, which is well documented.[69] The synergistic effect between 1L-MoS_2 and InAs@ZnSe NCs leads to an increase in responsivity compared to pristine MoS_2. In the UV and visible spectrum, MoS_2 itself contributes to the responsivity.[14] However, with the incorporation of InAs@ZnSe NCs alongside MoS_2, light absorption is significantly enhanced. As reported by many other groups, this increase in light absorption leads to a substantial increase in responsivity.[49,70] The combined structure effectively traps light energy, further enhancing device performance.[27] These findings are in line with previous reports and underscore the effectiveness of the composite structure in improving light absorption and device performance in UV visible and Infrared windows.[27,49,69,71] The enhanced response in the infrared region (700 and 850 nm), where 1L-MoS_2 is transparent,[30] implies that InAs@ZnSe NCs absorb light within this range and interact with MoS_2 to generate a photocurrent, as shown in Figure 5c. The photocurrent is observed in 1L-MoS_2 at 700 nm, which is very weak (Figure 4a), suggesting that InAs@ZnSe also plays a significant role in this spectral region. Instead, at 850 nm excitation, only InAs@ZnSe

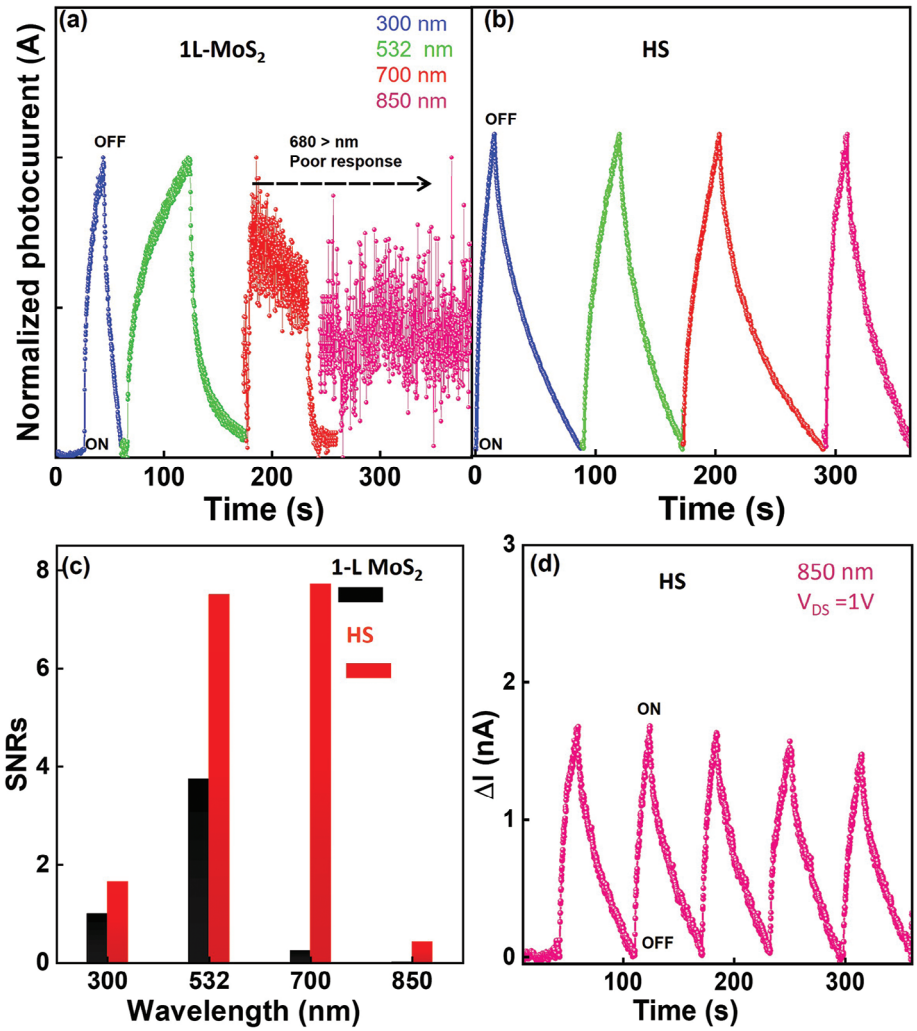

Figure 4. The dynamic photoresponse (I–t) of pristine a) 1L-MoS_2 and b) InAs@ZnSe/MoS_2 HS under similar conditions. Power densities at wavelengths of 300 nm (1.53 mW cm^{-2}), 532 nm (0.0165 mW cm^{-2}), 700 nm (0.7 mW cm^{-2}), and 850 nm (2.55 mW cm^{-2}) were applied with V_{ds} = 1 V and V_g = 0 V. c) The signal-to-noise ratio (derived from a) for pristine 1L-MoS_2 and InAs@ZnSe/MoS_2 HS (derived from b) under the same conditions is illustrated. d) The multiple dynamic photoresponse under 850 nm excitation with a power density of 2.55 mW cm^{-2}.

NCs absorb the photons, hence, playing a major role in increasing the photoresponse of 1L-MoS_2. The detectivity (D^*) of the pristine 1L-MoS_2 and InAs@ZnSe/MoS_2 HS was calculated using the formula provided above. It was found that the detectivity of 1L-MoS_2 is on the order of 10^{10} Jones, whereas for InAs@ZnSe/MoS_2 HS, it significantly improves to the order of 10^{11} Jones. The spectral variation of D^* follows a similar trend to R[72] given in Figures S10a,b (Supporting Information). The response time of the device was calculated, and it was found the rise time (τ_r), and fall time (τ_f) in order of a few seconds (≈4s to 13s for InAs@ZnSe/MoS_2 HS). A detailed discussion is provided in Supporting Information Section 1.12 and Figures S11a–d (Supporting Information).

A comparison table is provided in **Table 1** below, where we have compared our device performance with other broad-band-based reported results.

The device stability is monitored and it has been observed that after 6 months, the dark current (Figure S12, Supporting Information) remains approximately consistent with its initial level, indicating the robustness of the InAs@ZnSe/MoS_2 HS. To explore further the device mechanism and existence of trap states, we have calculated the α value[81]

$$\Delta I = b \cdot P^{\alpha} \quad (4)$$

where α is the dimensionless exponent of the power law that gives information about the trap (for minority carriers) present in the photodetection system, and b is a parameter related to the photodetector.[81] It is known that when the α value is 1, it indicates the device is free from traps. The device responsivity remains constant with illumination power, which is known as the photoconductive effect. When α is less than 1, it indicates that the photodetector device presents trap states, and the responsivity depends sub-linearly on power density.[82]

However, the MoS_2 and the InAs@ZnSe/MoS_2 HS do not reach a steady state (A detailed discussion is given in Section

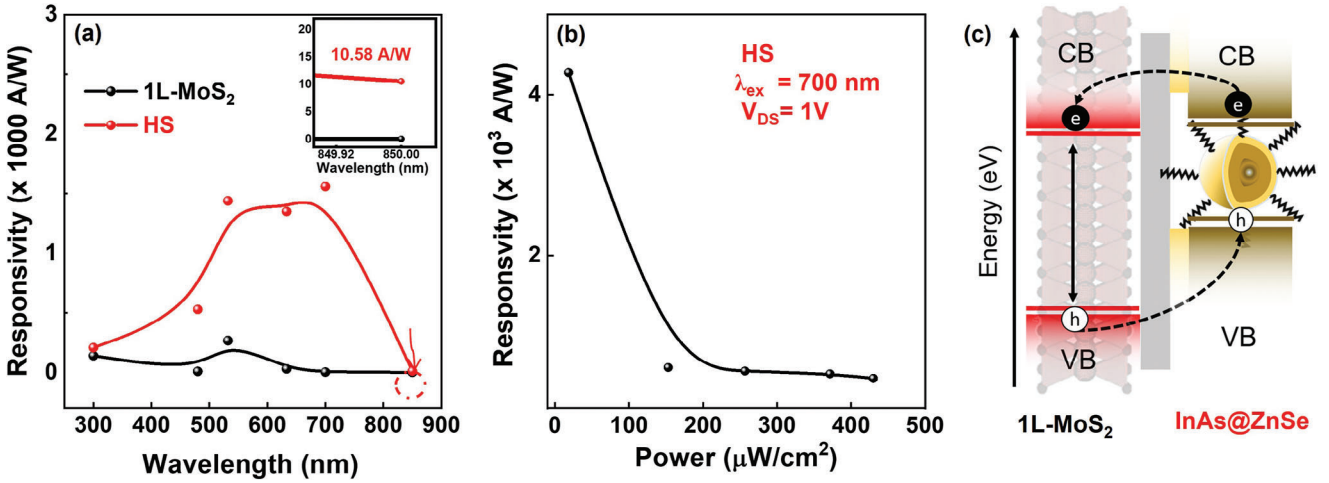

Figure 5. a) Responsivity as a function of wavelengths for pristine 1L- MoS_2 and InAs@ZnSe/MoS_2 HS under the same conditions as depicted in Figure 4a (for 480 nm (0.45 mW cm^{-2}) and 633 nm (0.53 mW cm^{-2})), b) responsivity as a function of power for the InAs@ZnSe/MoS_2 HS device at a wavelength of 700 nm under fixed bias voltage (V_{ds} = 1 V). c) The schematic illustration depicts the process of charge transfer between 1L-MoS_2 and InAs@ZnSe NCs HS. The lines connecting the data points (a, and c) serve as a guide to the eye only.

1.14, Figure S13–S15 Supporting Information), rendering it impractical to study power-dependent photocurrent through this approach. Consequently, we conducted a qualitative investigation of transient photocurrent. The time derivative of the photoexcited charge density (n), once the illumination is stopped, is governed by a function of n itself[83]

$$\frac{dn}{dt} = g(n) \tag{5}$$

Assuming that the photocurrent is proportional to n, the function $g(n)$ can be determined from the time dependence of ΔI during the decay measurement. In Figure S16 a,b (Supporting Information) we show the derivative of photocurrent ($\frac{d\Delta I}{dt}$) plotted against ΔI subsequent to the light stop. We found that for MoS_2 a polynomial of the 2.68 order, while for HS a polynomial of the 2.66 order, both provide an excellent fit to the data (as indicated by the dashed line in Figure S16 a,b, Supporting Information)

Table 1. Comparison of the device performance of the InAs@ZnSe/MoS2 hybrid with its individual counterparts.

Materials	Max. responsivity [A/W]	Max. detectivity [D^*]	Response time [minimum]	Gating [V_g]	Working wavelength [nm]	Refs.
MoS_2	880	–	4 s	Yes	400–680	[14]
MoS_2	0.0075	–	50 ms	Yes	400–670	[73]
Multi-layer MoS_2	>0.1	10^{11}	–	Yes	450–850	[74]
Perovskite /MoS2	16.8	10^{13}	4 ms	No	200–1100	[75]
PbS/MoS2	≈10^6	10^{14}	0.3s	Yes	400–1500	[26]
CdSe/MoS_2	≈10^{-2}		–	No	–	[76]
ZnCdSe/MoS_2	10^4	10^{12}	0.3s	No	400–750	[65]
CQD/MoS_2	0.018	–	0.57s	No	365–780	[27]
Au/MoS_2	≈10^3	10^{11}	0.4s	Yes	660–740	[23]
$CuInSe_2$/MoS_2	10^2	10^{12}	0.8s	Yes	355–1064	[49]
GQD/MoS2	10^4	–	70 ms	Yes	405	[71]
ZnO/MoS_2	2.7	–	–	No	254 nm	[77]
n-Dope MoS_2	99.9	10^{12}	5.2 s	Yes	450–750	
Au@MoS_2	22.3	–	20 ms	Yes	360–660	[18]
MoO_3/MoS_2/Si	0.16	10^{11}	600 ms	No	400–700	[29]
MoO_3@MoS_2/Si	0.0092	10^{10}	–	No	Aster light	[28]
Pt-MoS_2	0.002	10^6		No	1064	[78]
MoS_2(1−x)Se_2x ternary alloy	2.06	–	18s	No	532	[79]
Large area MoS_2	10^{-4}	10^8	33 ms	No	532	[80]
InAs@ZnSe/1L-MoS_2	≈ 10^3	≈10^{11}	4s	No	300–850	This Work

suggesting that the differential equation governing generation-recombination under illumination is[83]

$$\frac{dn}{dt} = F - R_r n^{\frac{1}{\alpha}} \quad (6)$$

here, F denotes the generation rate due to incident light, while R_r represents a constant controlling the recombination rate. At steady state conditions ($\frac{dn}{dt} = 0$), solving Equation (6) yields a dependence of ΔI on F as $\Delta I \approx n \approx F^{\alpha}$, with $\alpha_{MoS_2} = 0.373$ for pristine MoS_2 and $\alpha_{HS} = 0.376$ for InAs@ZnSe/MoS_2 HS. The non-unity values of α for both 1L-MoS_2 and HS indicate that the photoconductive response in both materials is predominantly governed by the photogating effect.[13] The observed power-law dependence is attributed to the dynamics of traps and recombination centers facilitating photoconduction in nanostructured materials. Nonlinear variations in photocurrent with light intensity may arise from the distribution of traps and recombination centers within the band gap or the saturation of these states under intense light excitation, which occur similarly in both systems.

3. Conclusion

In summary, our study successfully demonstrates the integration of InAs@ZnSe NCs with monolayer MoS_2 via a straightforward spin-coating process, thereby extending the light detection window of the latter. Initially, Raman and PL's studies unveiled charge transfer and doping in MoS_2 alongside the formation of an InAs@ZnSe /MoS_2 HS with a type II band alignment. We further validated this charge transfer using transient absorption spectroscopy, offering direct evidence of charge transfer and its optical properties. Subsequently, we confirmed our findings by implementing an InAs@ZnSe/MoS_2 heterostructure via transport characterization. The device exhibited a broadband photoresponse ranging from 300 to 850 nm with responsivity $\approx 10^3$ A/W. and Detectivity $\approx 10^{11}$ Jones. The signal-to-noise ratio increases by 3 to 4 orders for 700 and 850 nm excitation. This enhancement in photoresponse and improving the SNR is attributed to MoS_2 doping and increased absorption, which helps eliminate defect and trap states while promoting the photogating effect. Overall, this work establishes a foundation for combining 0D InAs@ZnSe with 2D MoS_2, bridging fundamental insights into charge transfer physics with potential optoelectronic applications.

4. Experimental Section

Materials: MoS_2 bulk crystals were purchased from 2D semiconductors and other chemicals.Indium(III) chloride ($InCl_3$, 99.999%, Sigma–Aldrich), zinc(II) chloride (ZnC_{l2}, 99.999%, Sigma–Aldrich), tris(dimethylamino)arsine (amino-As, 99%, Strem), alane N,Ndimethylethylamine complex solution (DMEA–AlH_3, 0.5 M solution in toluene, Sigma–Aldrich), selenium powder (Se, 99.99%, Strem), oleylamine (OA, 98%, Sigma–Aldrich), tri-n-octylphosphine (TOP, 97%, Strem), toluene (anhydrous, 99.8%, Sigma–Aldrich), ethanol (anhydrous, 99.8%, Sigma–Aldrich).

Synthesis of InA NCs Synthesis: InAs@ZnSe NCs were synthesized using our previously reported method with minor modifications.[39,41] The arsenic precursor was prepared by dissolving 0.2 mmol of amino-As in 0.5 mL of degassed OA at 40 °C for 5 min in an N_2-filled glovebox. For 1 M TOP-Se precursor, 10 mmol of selenium powder was mixed with 10 mL of TOP in an N_2-filled glovebox at 250 °C for 30 min. For the synthesis of InAs core NCs, 0.2 mmol of $InCl_3$, 4 mmol of $ZnCl_2$, and 5 mL of OA were degassed at 120 °C under vacuum for 40 min. The mixture was heated up to 180 °C under N_2 for 30 min, and then it was cooled down to 120 °C and degassed under vacuum for an extra 30 min. The mixture was heated up to 240 °C under N_2, and the As precursor was injected into the flask quickly followed by the injection of 1.2 mL of the DMEA-AlH_3 toluene solution. Then, the temperature was increased to 300 °C and the reaction was carried out for 15 min. The flask was cooled down to 90 °C by removing the heating mantle. For the synthesis of InAs NCs, 1 mL of 1 M TOP-Se precursor was injected into the above InAs core NCs solution, and the flask was heated up to 300 °C and kept at this temperature for 10 min. The NCs were purified by dispersion in toluene and precipitation with ethanol. The final product was dispersed in toluene.

Monolayer MoS_2 Synthesis: We utilized the gold-assisted method to exfoliate the monolayer MoS_2 mechanically. These monolayer MoS_2 sheets were then transferred onto a cleaned SiO_2/Si substrate. Further details regarding the exfoliation process can be found in our previous work and Section 1.1 (Supporting Information) ESI.[32]

Device Fabrication: Electrical contacts were fabricated using UV-photolithography. Detailed descriptions and step-by-step instructions for device fabrication can be found in the Electronic Supplementary Information (ESI) Section 1.2 (Supporting Information).

InAs@ZnSe/MoS_2 Heterostructure (HS) Formation: After successfully obtaining the monolayer MoS_2 and high quantum yield InAs NCs, it was proceeded by spin-coating the InAs NCs onto the MoS_2 to form a heterostructure. This was accomplished using a spin-coater at 2000 RPM for 1 min.

Characterization: The Helios Nanolab 650 by FEI was employed for imaging the nanocrystals and transition metal dichalcogenide (TMDC) monolayers. No specific sample preparation was required for SEM imaging. AFM was performed with the Veeco Multimode/Nanoscope IV system in tapping mode. Data processing was made with the open-source software Gwyddion. The Renishaw Raman system was utilized to collect high-resolution Raman spectroscopy data. The measurements were carried out using a 2400 grating, with a 532 nm excitation wavelength and a power of 0.3 mW, employing a 50X objective lens under ambient conditions.

For optical pictures, we utilized a Zeta Profilometer to capture the images. Micro-photoluminescence: The second harmonic of the pump in a chameleon compact OPO laser was used for excitation. Specifications are 532 nm pulsed light with a pulse width of 200 fs, and a repetition rate of 80 MHz. The excitation laser was coupled into IX83 Olympus microscope and focused on the sample with 50X (N.A 0.8) microscope objective lens. The photoluminescence light was collected and collimated by the same objective lens, which was used for detection. The PL light was focused on slit of a Czerny-Turner HRS-500 spectrometer (Princeton Instruments) to resolve the light spectrally. The spectrally resolved light was detected and read using PIXIS CCD camera and Lightfield software (Princeton Instruments).

The ultrafast transient absorption spectroscopy was conducted using a Ytterbium-based laser system (Pharos-SP-HP, Light Conversion). The pump wavelengths at 532 and 800 nm were obtained through a commercial optical parametric amplifier system endowed with a second harmonic generation module (Orpheus, Light Conversion) while the supercontinuum white light was generated by focusing a portion of the laser output (at ≈1030 nm) onto a sapphire crystal. The pulse duration of the pump pulses was ≈160 fs while the instant response function, given by the cross-correlation between pump and probe, was estimated experimentally in ≈230 fs. The delay between the pump and probe pulses was tuned by changing the length of the optical path of the probe. All the TA spectra were acquired through the Harpia-TA (Light Conversion) system. Experiments were performed at 50 kHz while the acquisition was obtained using a chopper with frequency of ≈78 Hz. The spot size of the pump at sample was measured in ≈120 µm while the probe diameter was ≈ 60 µm. In the TA spectra and map presented, the chirp of the probe pulse was corrected using Carpetview software (Light Conversion).

Transmission electron microscopy (TEM) image was collected by on a JEOL JEM-1400Plus microscope with a thermionic gun (W filament) operated at an acceleration voltage of 120 kV. The diluted NCs solution was drop-cast onto copper TEM grid with an ultrathin carbon. The absorption spectrum was recorded on a Varian Cary 5000 UV-vis–NIR spectrophotometer. The steady-state PL measurement was carried out on an Edinburgh Instruments FLS920 fluorescence spectrometer equipped with an Xe lamp. The sample was prepared by diluting NC samples in 3 mL of toluene in 1 cm path-length quartz cuvettes with airtight screw caps in an N_2-filled glovebox.

The device's electrical characterization was conducted using a Suss MicroTec probe station equipped with an Olympus microscope. DC voltage and current measurements were performed using a Keithley 2614B source meter. To excite the sample, a tunable laser from NKT Photonics, with a wavelength range of 480–700 nm, was coupled with a fiber cable from Thor Labs. For 850 nm excitation, we utilized a Thor Labs multi-channel fiber-coupled laser source. Additionally, a Thor Lab LED was employed for 300 nm for UV excitation. An IR card from Thor Labs was used to visualize the laser spot for 850 nm light. Power measurements were carried out using a Thor Lab power meter (PM130D). All measurements were performed under ambient conditions.

Supporting Information

Supporting Information is available from the Wiley Online Library or from the author.

Acknowledgements

A.A. and M.K.T. contributed equally to this work. A.A., M.K.T., N.T., N.P., N.C., and I.K. acknowledge the support of the European Union's Horizon 2020 European Research Council, under grant agreement no. 850875 (I.K.) (Light-DYNAMO) and A.A. and I.K. acknowledge the Horizon Europe European Research Council Proof of Concept under grant agreement no. 101069295 (CONDINKS project). I.K. acknowledges the European Union's Horizon 2020 Research and Innovation program under grant agreement no. 101017821 (I.K.) (LIGHT-CAP). A.T. and J.S.P.C. would like to acknowledge the support from the European Research Council (ERC) under the European Union's Horizon 2020 research and innovation program "REPLY ERC-2020-COG" Grant agreement No. 101002422. D.Z. and L.M. acknowledge funding from the program MiSE-ENEA under the Grant "Italian Energy Materials Acceleration Platform – IEMAP". N.C. acknowledges the European Union's Horizon Europe research and innovation program under the Marie Sklodowska-Curie grant agreement no. 101109662 (2DTWIST). M.K.T. acknowledges the European Union's Horizon Europe research and innovation program under the Marie Sklodowska-Curie grant agreement no. 101152448 (INFRALIGHT).

Open access publishing facilitated by Istituto Italiano di Tecnologia, as part of the Wiley - CRUI-CARE agreement.

Conflict of Interest

The authors declare no conflict of interest.

Data Availability Statement

The data that support the findings of this study are available from the corresponding author upon reasonable request.

Keywords

broadband, Inas@Znse, MoS_2, photodetector, transient absorption spectroscopy

Received: June 7, 2024
Revised: August 14, 2024
Published online: September 6, 2024

[1] T. Tan, X. Jiang, C. Wang, B. Yao, H. Zhang, *Adv. Sci.* **2020**, *7*, 2000058.
[2] Z. Xing, H. Xiaozong, Y. Jing, L. Shiyuan, S. Zhaowei, Z. Qi, L. Huiqiao, M. Ying, X. Hua, Z. Tianyou, *Adv. Funct. Mater.* **2023**, *33*, 2302474.
[3] B. Guo, Q. Xiao, S. Wang, H. Zhang, *Laser Photonics Rev.* **2019**, *13*, 1800327.
[4] Y. Liu, X. Duan, Y. Huang, X. Duan, *Chem. Soc. Rev.* **2018**, *47*, 6388.
[5] D.-B. Seo, Y. M. Kwon, J. Kim, S. Kang, S. Yim, S. S. Lee, E.-T. Kim, W. Song, K.-S. An, *ACS Appl. Mater. Interfaces* **2024**, *16*, 28613.
[6] J. Pu, T. Takenobu, *Adv. Mater.* **2018**, *30*, 1707627.
[7] H.-L. Liu, C.-C. Shen, S.-H. Su, C.-L. Hsu, M.-Y. Li, L.-J. Li, *Appl. Phys. Lett.* **2014**, *105*, 201905.
[8] S. S. Sunku, D. Halbertal, R. Engelke, H. Yoo, N. R. Finney, N. Curreli, G. Ni, C. Tan, A. S. McLeod, C. F. B. Lo, C. R. Dean, J. C. Hone, P. Kim, D. N. Basov, *Nano Lett.* **2021**, *21*, 1688.
[9] A. Splendiani, L. Sun, Y. Zhang, T. Li, J. Kim, C.-Y. Chim, G. Galli, F. Wang, *Nano Lett.* **2010**, *10*, 1271.
[10] J. Wang, V. Malgras, Y. Sugahara, Y. Yamauchi, *Nat. Commun.* **2021**, *12*, 3563.
[11] M. Brotons-Gisbert, J. P. Martínez-Pastor, G. C. Ballesteros, B. D. Gerardot, J. F. Sánchez-Royo, *Nanophotonics* **2018**, *7*, 253.
[12] M. Bernardi, M. Palummo, J. C. Grossman, *Nano Lett.* **2013**, *13*, 3664.
[13] W.-R. Syong, J.-H. Fu, Y.-H. Kuo, Y.-C. Chu, M. Hakami, T.-Y. Peng, J. Lynch, D. Jariwala, V. Tung, Y.-J. Lu, *ACS Nano* **2024**, *18*, 5446.
[14] O. Lopez-Sanchez, D. Lembke, M. Kayci, A. Radenovic, A. Kis, *Nat. Nanotechnol.* **2013**, *8*, 497.
[15] A. Chetia, J. Bera, A. Betal, S. Sahu, *Mater. Today Commun.* **2022**, *30*, 103224.
[16] M.-Y. Li, M. Yu, S. Jiang, S. Liu, H. Liu, H. Xu, D. Su, G. Zhang, Y. Chen, J. Wu, *Mater. Horiz.* **2020**, *7*, 905.
[17] Y. Li, Z. Li, C. Chi, H. Shan, L. Zheng, Z. Fang, *Adv. Sci.* **2017**, *4*, 1600430.
[18] Y. Li, J. G. DiStefano, A. A. Murthy, J. D. Cain, E. D. Hanson, Q. Li, F. C. Castro, X. Chen, V. P. Dravid, *ACS Nano* **2017**, *11*, 10321.
[19] M. K. Thakur, C.-Y. Fang, Y.-T. Yang, T. A. Effendi, P. K. Roy, R.-S. Chen, K. K. Ostrikov, W.-H. Chiang, S. Chattopadhyay, *ACS Appl. Mater. Interfaces* **2020**, *12*, 28550.
[20] A. Gupta, M. K. Thakur, T. A. Effendi, R.-S. Chen, H.-Y. Cheng, K.-H. Lin, M. Bouras, D. S. Tomar, H. Y. Kuo, S. Chattopadhyay, *Chem. Eng. J.* **2021**, *420*, 127608.
[21] M. H. Kang, S. H. Kim, S. Jang, J. E. Lim, H. Chang, K. Kong, S. Myung, J. K. Park, *RSC Adv.* **2018**, *8*, 28447.
[22] D. Wang, B. Han, G. Wang, B. Liu, S. Ma, B. Xu, G. Li, *J. Phys. D: Appl. Phys.* **2023**, *56*, 445101.
[23] D. Lu, Y. Chen, L. Kong, C. Luo, Z. Lu, Q. Tao, W. Song, L. Ma, Z. Li, W. Li, L. Liu, Q. Li, X. Yang, J. Li, J. Li, X. Duan, L. Liao, Y. Liu, *Small* **2022**, *18*, 2107104.
[24] R. A. Yotter, D. M. Wilson, *IEEE Sens. J.* **2003**, *3*, 288.
[25] A. Gupta, S. Ghosh, M. K. Thakur, J. Zhou, K. (Ken) Ostrikov, D. Jin, S. Chattopadhyay, *Prog. Mater. Sci.* **2021**, *121*, 100838.
[26] D. Kufer, I. Nikitskiy, T. Lasanta, G. Navickaite, F. H. L. Koppens, G. Konstantatos, *Adv. Mater.* **2015**, *27*, 176.
[27] P. Sahatiya, S. S. Jones, S. Badhulika, *Appl. Mater. Today* **2018**, *10*, 106.
[28] S. Gunasekaran, R. Marnadu, D. Thangaraju, J. Chandrasekaran, H. H. Hegazy, H. H. Somaily, A. Durairajan, M. A. Valente, M. Elango, V. R. Minnam Reddy, *Mater. Sci. Semicond. Process.* **2021**, *135*, 106097.
[29] S. Pal, S. Mukherjee, M. Nand, H. Srivastava, C. Mukherjee, S. N. Jha, S. K. Ray, *Appl. Surf. Sci.* **2020**, *502*, 144196.

[30] K. Abbas, P. Ji, N. Ullah, S. Shafique, Z. Zhang, M. F. Ameer, S. Qin, S. Yang, *Microsyst. Nanoeng.* **2024**, *10*, 81.
[31] J. Luo, G. S. Selopal, X. Tong, Z. Wang, *Electron* **2024**, *2*, 30.
[32] Y. Ma, Y. Li, H. Wang, M. Wang, J. Wang, *Chip* **2023**, *2*, 100032.
[33] S.-J. Jeong, S. Cho, B. Moon, J. A. Teku, M.-H. Jeong, S. Lee, Y. Kim, J.-S. Lee, *ACS Appl. Mater. Interfaces* **2023**, *15*, 5432.
[34] R. Zhang, X. Ma, C. An, D. Zhang, D. Sun, X. Hu, J. Liu, *2D Mater.* **2019**, *6*, 035033.
[35] H. Lu, G. M. Carroll, N. R. Neale, M. C. Beard, *ACS Nano* **2019**, *13*, 939.
[36] H. Bahmani Jalali, L. De Trizio, L. Manna, F. Di Stasio, *Chem. Soc. Rev.* **2022**, *51*, 9861.
[37] R. Xie, K. Chen, X. Chen, X. Peng, *Nano Res.* **2008**, *1*, 457.
[38] D. Zhu, F. Bellato, H. Bahmani Jalali, F. Di Stasio, M. Prato, Y. P. Ivanov, G. Divitini, I. Infante, L. De Trizio, L. Manna, *J. Am. Chem. Soc.* **2022**, *144*, 10515.
[39] M. De Franco, D. Zhu, A. Asaithambi, M. Prato, E. Charalampous, S. Christodoulou, I. Kriegel, L. De Trizio, L. Manna, H. Bahmani Jalali, F. Di Stasio, *ACS Energy Lett.* **2022**, *7*, 3788.
[40] F. Ning, D. Wang, Y.-X. Feng, L.-M. Tang, Y. Zhang, K.-Q. Chen, *J. Mater. Chem. C* **2017**, *5*, 9429.
[41] D. Zhu, H. Bahmani Jalali, G. Saleh, F. Di Stasio, M. Prato, N. Polykarpou, A. Othonos, S. Christodoulou, Y. P. Ivanov, G. Divitini, I. Infante, L. De Trizio, L. Manna, *Adv. Mater.* **2023**, *35*, 2303621.
[42] N. Petrini, A. Asaithambi, L. Rebecchi, N. Curreli, *Opt. Mater.: X* **2023**, *19*, 100255.
[43] N. Petrini, E. Peci, N. Curreli, E. Spotorno, N. Kazemi Tofighi, M. Magnozzi, F. Scotognella, F. Bisio, I. Kriegel, *Adv. Opt. Mater.* **2024**, *12*, 2303228.
[44] F. Liu, W. Wu, Y. Bai, S. H. Chae, Q. Li, J. Wang, J. Hone, X.-Y. Zhu, *Science (1979)* **2020**, *367*, 903.
[45] M. Velický, G. E. Donnelly, W. R. Hendren, S. McFarland, D. Scullion, W. J. I. DeBenedetti, G. C. Correa, Y. Han, A. J. Wain, M. A. Hines, D. A. Muller, K. S. Novoselov, H. D. Abruña, R. M. Bowman, E. J. G. Santos, F. Huang, *ACS Nano* **2018**, *12*, 10463.
[46] G. Eda, H. Yamaguchi, D. Voiry, T. Fujita, M. Chen, M. Chhowalla, *Nano Lett.* **2011**, *11*, 5111.
[47] B. Radisavljevic, A. Radenovic, J. Brivio, V. Giacometti, A. Kis, *Nat. Nanotechnol.* **2011**, *6*, 147.
[48] H. Li, Q. Zhang, C. C. R. Yap, B. K. Tay, T. H. T. Edwin, A. Olivier, D. Baillargeat, *Adv. Funct. Mater.* **2012**, *22*, 1385.
[49] T. Shen, F. Li, Z. Zhang, L. Xu, J. Qi, *ACS Appl. Mater. Interfaces* **2020**, *12*, 54927.
[50] M.-L. Tsai, S.-H. Su, J.-K. Chang, D.-S. Tsai, C.-H. Chen, C.-I. Wu, L.-J. Li, L.-J. Chen, J.-H. He, *ACS Nano* **2014**, *8*, 8317.
[51] S. Kim, S. Yeon, M. Lee, J. Jin, S. Shin, N. Gwak, I. Jeong, H. Jang, G. W. Hwang, N. Oh, *NPG Asia Mater* **2023**, *15*, 30.
[52] D. Panda, M. Ranjan Mantri, R. Kumar, D. Das, R. Saha, S. Chakrabarti, *Appl. Surf. Sci.* **2023**, *607*, 154948.
[53] V. Varade, G. Haider, L. Pirker, J. Panda, J. Sykora, O. Frank, M. Kalbac, J. Vejpravova, *2D Mater.* **2023**, *10*, 025024.
[54] V. Varade, G. Haider, A. Slobodeniuk, R. Korytar, T. Novotny, V. Holy, J. Miksatko, J. Plsek, J. Sykora, M. Basova, M. Zacek, M. Hof, M. Kalbac, J. Vejpravova, *ACS Nano* **2023**, *17*, 2170.
[55] L. P. L. Mawlong, A. Bora, P. K. Giri, *Sci. Rep.* **2019**, *9*, 19414.
[56] A. Asaithambi, N. Kazemi Tofighi, N. Curreli, M. De Franco, A. Patra, N. Petrini, D. Baranov, L. Manna, F. Di Stasio, I. Kriegel, *Adv. Opt. Mater.* **2022**, *10*, 2200638.
[57] I. Kriegel, in *Proc. SPIE Photonics Europe, Strasbourg, France* **2022**, p. PC1214201.
[58] N. Petrini, M. Ghini, N. Curreli, I. Kriegel, *J. Phys. Chem. C* **2023**, *127*, 1576.
[59] R. Kesarwani, K. B. Simbulan, T.-D. Huang, Y.-F. Chiang, N.-C. Yeh, Y.-W. Lan, T.-H. Lu, *Sci. Adv.* **2024**, *8*, eabm0100.
[60] M. Guizzardi, M. Ghini, A. Villa, L. Rebecchi, Q. Li, G. Mancini, F. Marangi, A. M. Ross, X. Zhu, I. Kriegel, F. Scotognella, *J. Phys. Chem. Lett.* **2022**, *13*, 9903.
[61] S. Pan, F. Ceballos, M. Z. Bellus, P. Zereshki, H. Zhao, *2D Mater.* **2017**, *4*, 015033.
[62] C. Trovatello, F. Katsch, N. J. Borys, M. Selig, K. Yao, R. Borrego-Varillas, F. Scotognella, I. Kriegel, A. Yan, A. Zettl, P. J. Schuck, A. Knorr, G. Cerullo, S. D. Conte, *Nat. Commun.* **2020**, *11*, 5277.
[63] S. Deb, P. Bhattacharyya, P. Chakrabarti, H. Chakraborti, K. D. Gupta, A. Shukla, S. Dhar, *Phys. Rev. Appl.* **2020**, *14*, 34030.
[64] J.-H. Ahn, W. M. Parkin, C. H. Naylor, A. T. C. Johnson, M. Drndić, *Sci. Rep.* **2017**, *7*, 4075.
[65] S. Zhang, X. Wang, Y. Chen, G. Wu, Y. Tang, L. Zhu, H. Wang, W. Jiang, L. Sun, T. Lin, H. Shen, W. Hu, J. Ge, J. Wang, X. Meng, J. Chu, *ACS Appl. Mater. Interfaces* **2019**, *11*, 23667.
[66] A. Asaithambi, N. Kazemi Tofighi, M. Ghini, N. Curreli, P. J. Schuck, I. Kriegel, *Chem. Commun.* **2023**, *59*, 7717.
[67] S. Li, X. Chen, F. Liu, Y. Chen, B. Liu, W. Deng, B. An, F. Chu, G. Zhang, S. Li, X. Li, Y. Zhang, *ACS Appl. Mater. Interfaces* **2019**, *11*, 11636.
[68] D. Silvano, *Photodetectors, Devices, Circuits and Applications*, John Wiley & Sons, **2021**.
[69] S. Mukherjee, D. Bhattacharya, S. K. Ray, A. N. Pal, *Phys. Rev. Appl.* **2023**, *20*, 64010.
[70] Y. Li, J. D. Cain, E. D. Hanson, A. A. Murthy, S. Hao, F. Shi, Q. Li, C. Wolverton, X. Chen, V. P. Dravid, *Nano Lett.* **2016**, *16*, 7696.
[71] C. Chen, H. Qiao, S. Lin, C. M. Luk, Y. Liu, Z. Xu, J. Song, Y. Xue, D. Li, J. Yuan, W. Yu, C. Pan, S. P. Lau, Q. Bao, *Sci. Rep.* **2015**, *5*, 11830.
[72] M. K. Thakur, A. Gupta, M. Y. Fakhri, R. S. Chen, C. T. Wu, K. H. Lin, S. Chattopadhyay, *Nanoscale* **2019**, *11*, 9716.
[73] Z. Yin, H. Li, H. Li, L. Jiang, Y. Shi, Y. Sun, G. Lu, Q. Zhang, X. Chen, H. Zhang, *ACS Nano* **2012**, *6*, 74.
[74] W. Choi, M. Y. Cho, A. Konar, J. H. Lee, G.-B. Cha, S. C. Hong, S. Kim, J. Kim, D. Jena, J. Joo, S. Kim, *Adv. Mater.* **2012**, *24*, 5832.
[75] H. Wang, X. Wang, Y. Chen, S. Zhang, W. Jiang, X. Zhang, J. Qin, J. Wang, X. Li, Y. Pan, F. Liu, Z. Shi, H. Zhang, L. Tu, H. Wang, H. Long, D. Li, T. Lin, J. Wang, Y. Zhan, H. Shen, X. Meng, J. Chu, *Adv. Opt. Mater.* **2020**, *8*, 1901402.
[76] J. J. Gough, N. McEvoy, M. O'Brien, A. P. Bell, D. McCloskey, J. B. Boland, J. N. Coleman, G. S. Duesberg, A. L. Bradley, *Adv. Funct. Mater.* **2018**, *28*, 1706149.
[77] M.-A. Kang, S. Kim, I.-S. Jeon, Y. R. Lim, C.-Y. Park, W. Song, S. S. Lee, J. Lim, K.-S. An, S. Myung, *RSC Adv.* **2019**, *9*, 19707.
[78] Y. R. Lim, S. Jang, G. Bae, H. Y. Jeon, C. Jeon, D. S. Song, Y. M. Kwon, M. Jang, S. Yim, S. Myung, S. S. Lee, H. Chang, W. Song, K.-S. An, J. Lim, *Adv. Electron. Mater.* **2023**, *9*, 2300447.
[79] Y. R. Lim, J. K. Han, Y. Yoon, J.-B. Lee, C. Jeon, M. Choi, H. Chang, N. Park, J. H. Kim, Z. Lee, W. Song, S. Myung, S. S. Lee, K.-S. An, J.-H. Ahn, J. Lim, *Adv. Mater.* **2019**, *31*, 1901405.
[80] Y. M. Kwon, Y. R. Lim, G. Bae, D. S. Song, H. Jo, S. Y. Park, M. Jang, S. Yim, S. Myung, J. Lim, S. S. Lee, W. Song, *Small Methods* **2023**, *7*, 2300147.
[81] Q. Zhao, W. Wang, F. Carrascoso-Plana, W. Jie, T. Wang, A. Castellanos-Gomez, R. Frisenda, *Mater. Horiz.* **2020**, *7*, 252.
[82] N. Curreli, M. Serri, M. I. Zappia, D. Spirito, G. Bianca, J. Buha, L. Najafi, Z. Sofer, R. Krahne, V. Pellegrini, F. Bonaccorso, *Adv. Electron. Mater.* **2021**, *7*, 2001080.
[83] N. Curreli, M. Serri, D. Spirito, E. Lago, E. Petroni, B. Martín-García, A. Politano, B. Gürbulak, S. Duman, R. Krahne, V. Pellegrini, F. Bonaccorso, *Adv. Funct. Mater.* **2020**, *30*, 1908427.